PCCP

ROYAL SOCIETY OF CHEMISTRY

PAPER

View Article Online
View Journal | View Issue



Cite this: *Phys. Chem. Chem. Phys.*, 2022, **24**, 17535

# Coster–Kronig and super Coster–Kronig transitions from the Xe 4s core-hole state

Yasumasa Hikosaka *[a] and Stephan Fritzsche [bcd]

Received 11th May 2022,
Accepted 13th July 2022

DOI: 10.1039/d2cp02149h

rsc.li/pccp

Coster–Kronig and super Coster–Kronig transitions from the Xe 4s core-hole state are investigated by coincidence detection of all the emitted electrons and product ions. The branching ratios of the transitions are determined by analyzing the coincidence data and comparing them to calculations. Subsequent decay pathways following these first-step Auger decays are also clarified.



## I. Introduction

A core-hole state created by inner-shell photoionization of an atom in the soft X-ray regime predominantly undergoes Auger decay, leading to a dication or a higher charged ion. Although Auger spectroscopy is a standard method for studying such electron emission processes, it is often impossible to identify the individual Auger pathways, owing to the overlap of structures associated with different core-hole states and the large number of Auger steps. However, these core-hole states and Auger decay pathways can be disentangled if the photo- and Auger electrons are observed in coincidence.

To perform such electron coincidence measurements, magnetic bottle electron spectrometers have been found to be highly efficient. The introduction of this spectrometer into electron coincidence spectroscopy by Eland and co-workers occurred as early as in 1989.[1] Its practical use for highly efficient electron coincidence was demonstrated again by Eland *et al.* in 2003.[2] Since then, a good number of Auger decay processes in atoms have been revealed by electron coincidence spectroscopy using a magnetic bottle electron spectrometer,[3–11] where the Auger decays of the core-hole states in Xe have been the subject of intensive research. For the 4d core-hole state, for example, an electron coincidence measurement helped to reveal the direct and cascade double Auger pathways.[3] For the 4p core-hole states, which are known to be strongly mixed with the $4d^{-2}nf$ configurations,[12] the triple Auger decay was identified along with the single and double Auger decays.[5] The strong configuration mixing of the inner-shell holes with the virtual 4f excitations enhances the creation of 4d double core-hole states and multi-electron coincidence spectroscopy supported to clarify the associated sequential Auger decay.[11] The Auger decay from the next 4s core-hole state, in contrast, has not yet been studied in detail, while the decays from the 3d core-hole states were investigated and have revealed the most important quadruple Auger decay pathway.[9]

The power of multi-electron coincidence measurements can be boosted further if ions are also measured in coincidence, because various Auger processes that lead to different ion products can thus be distinguished by means of the additional coincidence. Indeed, efficient multi-electron–ion coincidence measurements of multiple Auger decays in Xe have been implemented with magnetic bottle electron spectrometers by applying the ion detection capability.[13,14] The branching ratios to product ions from individual core-hole states in Xe was investigated by a multi-electron–ion coincidence measurement.[13] In another study, the important quadruple Auger decay pathway from the 3d core-hole states could be clearly isolated by measuring the $Xe^{5+}$ ion in coincidence.[14]

In this study, the Auger decay of the $Xe^+$ $4s^{-1}$ state has been investigated by multi-electron–ion coincidence spectroscopy. This core-hole state is characterized by a wide natural width (2.9 eV[15]), which is caused by its Coster–Kronig (CK) and super Coster–Kronig (SCK) type electron emission. Conventional Auger spectroscopy can hardly provide information on the Auger decay paths from the $4s^{-1}$ state and the transition rates, because these 4s Auger structures are almost hidden behind the intense structures associated with other core-hole states. Until the present, however, the SCK transition to the $4d^{-2}$ states has only been identified in the multi-electron coincidence study of the 4d double photoionization.[11] A photoelectron–ion coincidence measurement revealed important formations of $Xe^{Z+}$ ions with $Z$ = 3–5 in the 4s Auger decay.[13] In the present work, the probabilities of the CK and SCK transitions and the

[a] *Institute of Liberal Arts and Sciences, University of Toyama, Toyama 930-0194, Japan. E-mail: hikosaka@las.u-toyama.ac.jp*
[b] *Theoretisch-Physikalisches Institut, Friedrich-Schiller-Universität Jena, D-07743 Jena, Germany*
[c] *GSI Helmholtzzentrum für Schwerionenforschung GmbH, D-64291 Darmstadt, Germany*
[d] *Helmholtz-Institut Jena, D-07743 Jena, Germany*

subsequent decay pathways after these transitions are analyzed and clarified by coincidence detections of the emitted electrons and product ions.

## II. Experimental

The experiment was carried out at the bending-magnet beamline BL4B of the UVSOR synchrotron facility. The electron storage ring was operated in the single-bunch and top-up injection mode, providing light pulses with 110 ps width and at a 178 ns repetition period. A magnetic bottle electron spectrometer[16] with ion detection capability[17] was employed in order to perform multi-electron–ion coincidence spectroscopy. Electrons emitted by the interaction between the photons and sample gases were captured over the entire $4\pi$ solid angle by an inhomogeneous magnetic field and then guided by the uniform magnetic field through a 1.5 m flight path to a microchannel plate detector of 90% open area ratio (Hamamatsu F2225-21P, funnel-processed).[14] According to the first electron detection after the incidence of each synchrotron light pulse, the interaction region was polarized by a pulsed electric field in order to extract ions toward the same detector. The heights of the high voltage pulses applied to the repeller and extractor electrodes[17] were 2 kV and 1.8 kV, respectively. The data acquisition scheme for measuring the long flight time of electrons and ions beyond the light pulse repetitions is described elsewhere.[17]

A multi-electron–ion coincidence measurement was implemented for Xe at a photon energy of 391.7 eV and with a bandwidth of $\sim$0.2 eV. This photon energy is high enough to ionize a 4s electron (binding energy of 213.32 eV[15]), but well below the binding energy of the deeper 3d electron. The measurements were carried out over five hours. The local pressure around the ionization region was estimated to be around $1 \times 10^{-3}$ Pa. The intensity of the incident light was adjusted so that the count rate becomes about 2000 counts per sec for this pressure. Fig. 1 shows a time-of-flight spectrum of all the detected electrons and ions. In this spectrum, electron structures appear within the first 3 μs, while the ions follow only after 8 μs. The energy resolution of the electrons was nearly constant at around 3% of the kinetic energy, over a kinetic energy range below 600 eV. The electron detection efficiency is fairly constant at around 70% in this kinetic energy range.[17] The peaks for the formations of different $Xe^{Z+}$ ions are well resolved in Fig. 1, where the $Xe^{Z+}$ ions ($Z > 6$) were produced by second-order light. It was estimated that the ion detection efficiencies for $Xe^{Z+}$ depend on the charge states and are 39%, 71%, 80%, 85% and 85% for $Z$ = 1–5, respectively.[17]

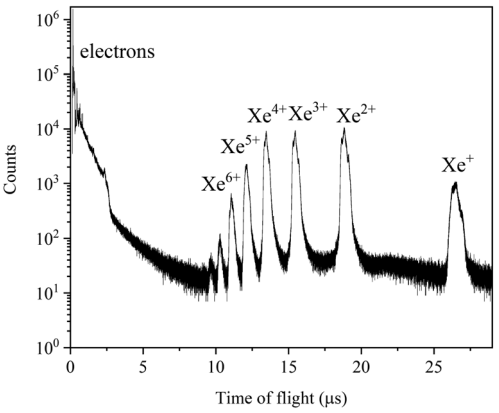


Fig. 1 Time-of-flight spectrum of all the electrons and ions produced for Xe at a photon energy of 391.7 eV.

## III. Computations

To model the decay of inner-shell ionized atoms, detailed computations of the level energies and transition rates are typically required for different hole-state configurations and charge states in order to predict the thresholds, branching fractions or even final ion charge-state distributions. Such cascade-type computations were performed below using JAC,[18] the Jena Atomic Calculator, which integrates different processes within a single framework and thus ensures good (self-) consistency of all generated data. This toolbox is based on the multi-configuration Dirac–Hartree–Fock (MCDHF) method[19] and has already been employed to analyze different cascades.[20]

However, the cascade computations are not free of limitations and usually require special care. Serious restrictions especially arise from missing bound–continuum correlations that cannot be incorporated by the present implementation, while the relativistic fine-structure splitting itself appears to be less relevant for predicting the CK and SCK branching ratios. For the 4s photoionization of Xe, in particular, parts of the $4d^{-2}nf$ and $4d^{-2}n'l'$ configurations lay as independent resonances in the continuum and cannot be captured by the bound-state density alone.[21] A further practical limitation in predicting reliable branching fractions arise moreover from the set-in of the 4f orbital contraction which, for Xe, roughly starts for doubly-ionized atoms and is quite difficult to control as the nuclear charge increases.[22] Unfortunately, therefore, a more complete treatment of missing – and especially (almost) all continuum–continuum – correlations is presently out of sight.

Below, we applied the JAC toolbox to calculate the energies, rates and branching fractions for initially 4s ionized Xe. In particular, the Auger and CK rates have been computed, by *ad hoc* incorporating the energy shifts of 4s and 4p holes due to their coupling to the continuum.[23] The main computational effort has been on the representation of the fine-structure levels at each step of the decay pathways as well as the transition amplitudes. To formalize such cascades, different cascade schemes and building blocks have been implemented[24] and now support elaborate calculations of inner-shell excited atoms and ions. We applied this recent implementation especially to analyze the formation of the 4s hole and its subsequent decay to the $4d^{-2}$, $4l^{-1}5l^{-1}$ and $5l^{-2}$ states. Because of the complexity of these double-hole states, however, the representation of the fine-structure levels needs to be restricted with regard to the

 

size of the wave function expansion and the ionic potential as seen by the emitted electrons, which need to be chosen separately for each final configuration of interest.[25] In the JAC toolbox, these two limitations are treated by specifying a hierarchy of cascade approaches for calculating the ionic level energies and state functions. In general, the size of such cascade computations increases rapidly with (i) the number of electrons that need to be replaced, and (ii) the depth of the cascade, *i.e.*, the maximum number of electrons that can be released, as well as (iii) the number of fine-structure transitions. Details of the implementation have been summarized elsewhere.[18,24]

## IV. Results and discussion

### IV-1. Photoelectron spectrum and ion branching ratio

Fig. 2 presents the photoelectron spectra as extracted from the total events as well as from those filtered by coincidences with different $Xe^{Z+}$ ions ($Z$ = 1–6). Photoelectron structures associated with photoionization from the Xe N and O shells are clearly seen in these spectra. The intensities of the coincidence spectra were corrected by the ion detection efficiencies, and thus the relative intensities of individual photoelectron structures in these spectra reflect the branching ratios from the corresponding core-hole states to these ion charge states. The ion branching ratios of the individual core-hole states have also been studied by Eland *et al.* using the same coincidence method.[13]

While the present study focuses on the decay of the $4s^{-1}$ state, some findings on the 4p structure seen in Fig. 2 are worth mentioning as well. The strongly correlated $4p^{-1}$ states[12] appear in the total electron spectrum as an anomalous photoelectron structure consisting of a peak around a kinetic energy of 245 eV and a distinct shoulder on the lower kinetic energy side. As already pointed out by Eland *et al.*,[13] determining the ion branching ratio of the 4p decay is not straightforward, since it varies greatly with the photoelectron range considered as the $4p^{-1}$ contribution. A multi-electron coincidence study reported a dominant $Xe^{3+}$ formation for the main 4p photoelectron peak,[5] which has indeed been confirmed by a recent calculation.[26] The shoulder part of the photoelectron structure is associated with double photoionization into the $4d^{-2}$ states, enhanced by virtual SCK transition[12] of $4p^{-1} \rightarrow 4d^{-2}\varepsilon f$ over several tens of electron volts.[11] The two 4d holes formed are predominantly filled sequentially,[11] resulting in the formation of $Xe^{4+}$. In practice, therefore, the shoulder part of the photoelectron structure essentially appears in the spectrum coincident with $Xe^{4+}$.

The total photoelectron spectrum in Fig. 2 exhibits a peak for the formation of the $4s^{-1}$ state at a kinetic energy of 178.5 eV. The peak width appears to be wider than the natural width of the $4s^{-1}$ state (2.9 eV[15]) owing to the spectrometer resolution. This peak lies on a large background to which double photoionization into $Xe^{2+}$ $4d^{-1}5l^{-1}$ and $4d^{-2}$ can contribute sizably. The formation of the $Z$ = 2–5 ions from the $4s^{-1}$ state is identified in the coincidence spectra, and the branching ratios for the product ions are estimated from the net peak

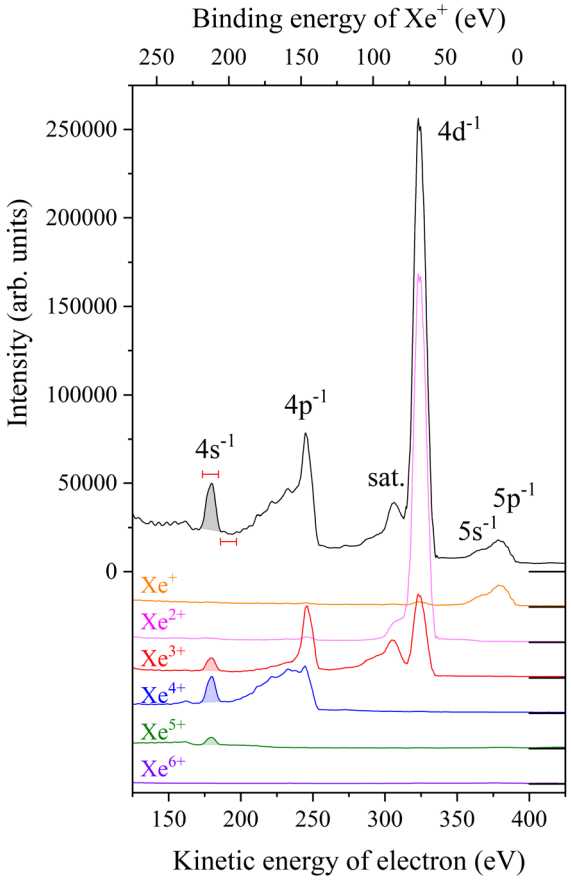


Fig. 2 Photoelectron spectra of Xe observed at a photon energy of 391.7 eV. The top spectrum is obtained for total events in the accumulated coincidence dataset, while the other spectra result from coincidence filters with individual $Xe^{Z+}$ ions ($Z$ = 1–6). The intensities of the coincidence spectra were corrected by the ion detection efficiencies. Two energy ranges for extractions (in red) of coincidence events related to the 4s decay and background processes are indicated for the top spectrum. "sat." denotes correlated satellite structures that likely occur due to 5p → *n*p shake-up contributions.

intensities in the coincidence spectra. They are found to be 1%, 27%, 55%, and 16% for $Z$ = 2, 3, 4 and 5, respectively. These values differ somewhat from the findings by Eland *et al.*,[13] which show a fairly even ratio among the $Z$ = 3–5 ions. The estimation by Eland *et al.*, based on the measurement at a photon energy only 37 eV above the 4s threshold, would have a difficulty due to the large background associated with Auger decays from the 4s and other core-hole states. In the meantime, the calculations by Kochur *et al.*[27] (1.0%, 16.5%, 77.4%, 5.1% for $Z$ = 2, 3, 4 and 5, respectively) show a similar trend to the present results. The Auger decay pathways forming these product ions will be revealed in this study. For a reference to follow the various Auger decay paths, the energy level diagram of the $Xe^{Z+}$ states ($Z$ = 1–5) lying below a binding energy of 220 eV is presented in Fig. 3.

### IV-2. Coster–Kronig and super Coster–Kronig transitions from the Xe 4s core-hole state

The Auger spectrum associated with the $4s^{-1}$ state, displayed in Fig. 4(a), was obtained by filtering coincidence events together

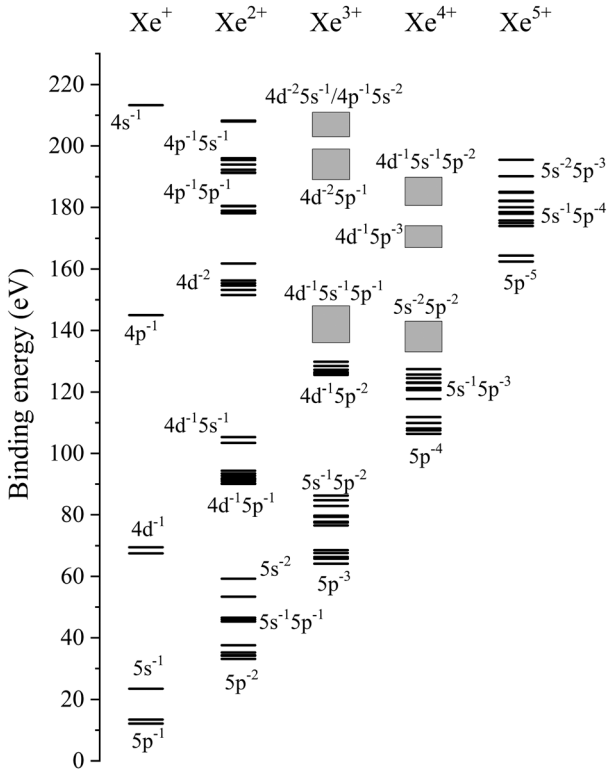


Fig. 3 Energy level diagram for the $Xe^{Z+}$ states ($Z$ = 1–5) lying below a binding energy of 220 eV. The energy levels for the $4p^{-1}5l^{-1}$ states are from the present calculations, while the other levels shown with horizontal bars are from the literature.[10,11,28] Boxes indicate the binding energy ranges for the corresponding Auger structures observed in the 3d Auger decay.[9]

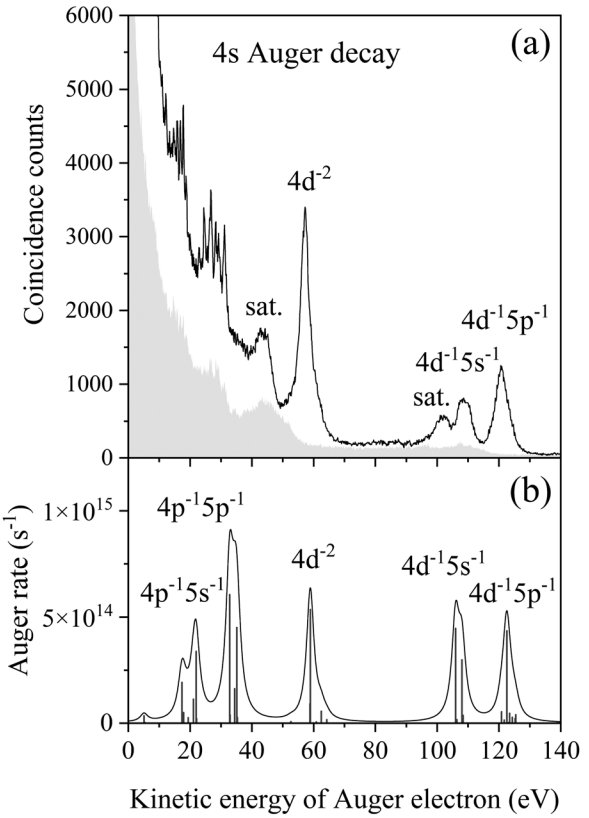


Fig. 4 (a) Auger spectrum (solid line) coincident with 4s photoelectron, and spectrum (shaded) delineating the background contribution. They are obtained in coincidence with an electron in either energy range indicated in Fig. 2. "sat." denotes correlated satellite structures analogue to Fig. 2. (b) Calculated Auger spectrum. The Auger rates for the formations of individual $Xe^{2+}$ levels are plotted with vertical bars, and the solid line shows convolution with the Lorenz function reflecting the natural width (2.9 eV[15]) of the $4s^{-1}$ state.

with the 4s photoelectron. Here, the coincidence spectrum extracted for a neighbored photoelectron range (as shown in Fig. 2) is presented as a shaded curve in order to account for the background contribution. Note that a simple subtraction of the reference spectrum from the 4s Auger spectrum does not yield the net 4s Auger structures. This is because the double photoionization into $Xe^{2+}$ states is an important part of the background that underlies the 4s peak and the high-energy selection of one of the two emitted photoelectrons leads to the $Xe^{2+}$ photoelectron structures at correspondingly lower kinetic energies in the reference spectrum. Apart from the spectral range in this figure, a weak structure, associated with the $N_1O_{1,2,3}O_{1,2,3}$ Auger transition to the $5l^{-2}$ states, should appear in the kinetic energy range of 160–180 eV with an intensity corresponding to the branching ratio of $Xe^{2+}$ production (1%); at the given photon energy, however, the Auger electrons are rather close in kinetic energy to the 4s photoelectron, and the coincidence of these events is almost lost owing to the detection deadtime.

In the 4s Auger spectrum, the $N_1N_{4,5}O_{1,2,3}$ CK transition to the $4d^{-1}5l^{-1}$ states leads to structures that are observed in the kinetic energy range of 90–130 eV. The most prominent peak at a kinetic energy of 57 eV can be assigned to the $N_1N_{4,5}N_{4,5}$ SCK transition to the $4d^{-2}$ states. The calculated Auger spectrum, displayed in Fig. 4(b), reproduces the energy positions of these structures reasonably well. While a broad peak is observed in the experimental spectrum around a kinetic energy of 43 eV, the corresponding transition could not be identified uniquely in the calculation. This structure should presumably be assigned to the $4d^{-2}$ satellites, which were not included in the present calculation and likely refer to 5p → $n$p shake-up contributions. The same applies for several $4d^{-1}4l^{-1}$ satellites which were not included in the present calculation either. While the calculation predicts the $N_1N_{2,3}O_{1,2,3}$ CK transitions to the $4p^{-1}5l^{-1}$ states at kinetic energies below 40 eV, identification of the corresponding structures is hindered in the experimental spectrum by the intense blending of lines from secondary Auger processes.

The branching ratios of the CK and SCK transitions in the total 4s decay can be determined by normalizing the net coincidence counts for the corresponding Auger structures in Fig. 4(a) with regard to the net 4s photoelectron counts in Fig. 2, where the detection efficiency for one Auger electron has to be compensated for in counting the coincidence. In this determination, the contribution from the background underlying the Auger structures has to be appropriately subtracted, which can be done by estimating the intensities from the

 

Table 1 Branching ratios of CK and SCK transitions in the 4s decay. The experimental values were determined from the Auger structures in Fig. 4, except the value for the transition to $4d^{-2}$ satellites, which was estimated by the total intensity of the island structures due to the stepwise decay seen in Fig. 6(b)

| Formed $Xe^{2+}$ states | Experiment | Present calculation | Hartree–Fock calculation [Kuc94] |
|---|---|---|---|
| $4d^{-1}5p^{-1}$ | 0.13 | 0.1512 | 0.0861 |
| $4d^{-1}5s^{-1}$ | 0.08 | 0.1876 | 0.0924 |
| $4d^{-1}5s^{-1}$ Satellites | 0.05 | | |
| $4d^{-2}$ | 0.28 | 0.1678 | 0.1152 |
| $4d^{-2}$ Satellites | 0.07 | | |
| $4p^{-1}5p^{-1}$ | ? | 0.4277 | 0.5446 |
| $4p^{-1}5s^{-1}$ | ? | 0.0657 | 0.1489 |

double photoionization structures in the shaded spectrum. As for the $4d^{-2}$ satellites, the branching ratio had to be obtained as described in the next section, since estimation of the background contribution was deemed dubious.

The branching ratios obtained are presented in Table 1, together with the present calculation and earlier Hartree–Fock calculation.[27] In addition to these relatively strong decays, the Auger decay into the $5l^{-2}$ states shares a fraction of 1%. In practice, however, the combined share of these allocated transitions is only 62% of the total 4s decay. It is expected that the CK transitions into the uncovered $4p^{-1}5l^{-1}$ states contribute significantly to the remaining 38% fraction in the 4s decay, as the calculation predicts the important contributions of the transitions. Apart from these single Auger transitions, direct double Auger decays into $Xe^{3+}$ states also contribute to the 4s decay. In fact, a weak structure associated with the direct double Auger decay into $4d^{-1}5l^{-2}$ states is observed in the present data, as presented in next section. A similar amount of the direct double Auger decay into the $4d^{-2}5l^{-1}$ states would also contribute to the 4s decay.

Although both the present and Hartree–Fock calculations reproduce the general trend in the experimental branching ratios reasonably well, they clearly underestimate the contribution from the SCK transition to $4d^{-2}$. Apart from missing correlations in the representation of the final states, this low branching fraction is likely associated with the localization of the 4s core-hole state and its coupling to the resonances in the continuum. As indicated before, furthermore, a series of computations showed that the SCK transition to $4d^{-2}$ states appears highly sensitive to a contraction of the 4d orbital as it results from a deliberate increase of the nuclear charge.

### IV-3. Subsequent decay after the Coster–Kronig and super Coster–Kronig transitions

$Xe^{2+}$ states that are produced by CK and SCK transitions can decay further, as these states still hold one or two core holes. To investigate the final product ions correlated to these $Xe^{2+}$ states, the Auger spectra coincident further with $Xe^{Z+}$ ($Z$ = 3–5) ions are extracted and presented in Fig. 5. The intensities of these coincidence spectra were corrected by the ion detection efficiencies, and in practice, the sum of these three spectra well agrees with the total Auger spectrum replotted at the top.

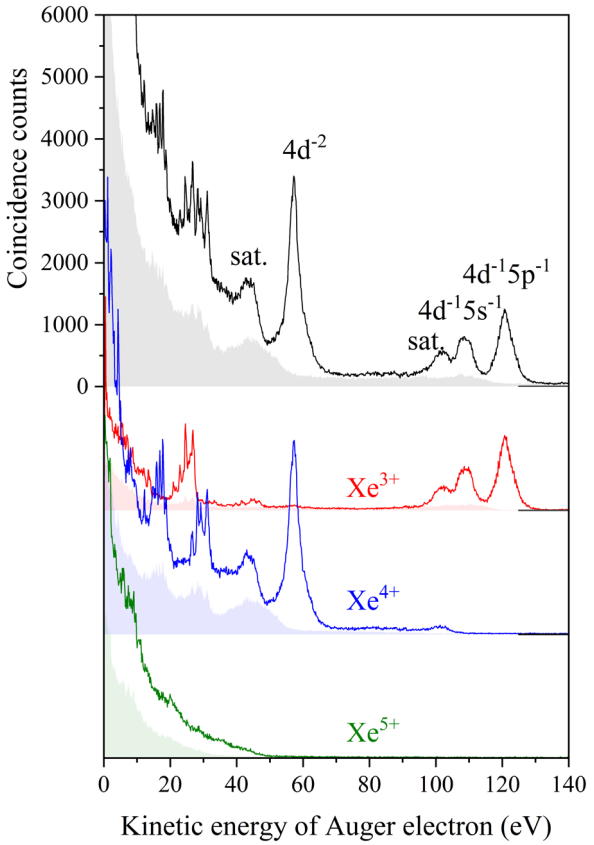


Fig. 5 Auger spectra (solid line) coincident with 4s photoelectron, and spectra (shaded) delineating the background contribution. The black spectra on top are the replots of those in Fig. 4(a), and the other spectra are derived by further coincidence with product ions of $Z$ = 3–5. The intensities of the spectra coincident with ions were corrected by the ion detection efficiencies. "sat." denotes correlated satellite structures analogue to Fig. 2.

This agreement implies that the ion detection efficiencies adopted are very reasonable.

The spectrum coincident with the $Xe^{3+}$ ion (red curve) shows the $N_1N_{4,5}O_{1,2,3}$ CK transition to the $4d^{-1}5l^{-1}$ states as well as structures lying below a kinetic energy of 50 eV. The $4d^{-1}5l^{-1}$ states are populated predominantly by subsequent Auger processes filling the 4d core-hole, while the structures below a kinetic energy of 50 eV in this spectrum are due to the consecutive processes. A detailed investigation of secondary Auger processes has already been conducted for the same processes contributing to the 4p decay.[5] The present study reveals that the $N_1N_{4,5}O_{1,2,3}$ CK transitions are indeed crucial for determining the $Xe^{3+}$ production. In practice, the fraction (26%) of the total $N_1N_{4,5}O_{1,2,3}$ CK transition for $Xe^{3+}$ formation is nearly identical to the branching ratio (27%) observed for the formation of $Xe^{3+}$ in the 4s decay.

The $4d^{-1}5l^{-1}$ satellites all lie around a kinetic energy of 100 eV and partly undergo double Auger decay to produce $Xe^{4+}$ states,[5] giving rise to the weak structure (corresponding to a 1% fraction in the 4s decay) in the spectrum coincident with the $Xe^{4+}$ ion (blue curve). A continuous intensity is found by

starting from the $4d^{-1}5l^{-1}$ satellites towards lower kinetic energies, which is due to the double Auger decay into the $4d^{-1}5l^{-2}$ states. The formed $Xe^{3+}$ states predominantly decay by further Auger processes, filling the 4d core-hole, and thus a double Auger structure appears in the $Xe^{4+}$ spectrum. The more pronounced structure in this spectrum belongs to the $4d^{-2}$ states and appears around a kinetic energy of 57 eV. The sequential fillings of the double 4d holes lead to the emissions of two additional Auger electrons,[11] resulting in the formation of the final $Xe^{4+}$ ions. The sharp peaks seen below the kinetic energy of 40 eV are mostly assigned to the stepwise decays of the $4d^{-2}$ states.

Fig. 6(a) presents a two-dimensional map showing the correlated energies of the two Auger electrons as emitted in the stepwise decays from the $4d^{-2}$ states. In this figure, several island structures are clearly seen and refer to level-to-level transitions from $Xe^{3+}$ to $Xe^{4+}$. The structures in the region $x$ = 25–35 eV, which are essentially the same as those observed in a previous study on 4d double photoionization,[11] are associated with the first-step transitions of $4d^{-2} \rightarrow 4d^{-1}5p^{-2}$ and the second-step transitions of $4d^{-1}5p^{-2} \rightarrow 5p^{-4}/5s^{-1}5p^{-3}$. Moreover, several intense islands in the region $x$ = 5–18 eV can be assigned to the transitions of $4d^{-2} \rightarrow 4d^{-1}5s^{-1}5p^{-1} \rightarrow 5s^{-2}5p^{-2}$.

The structure of the $4d^{-2}$ satellites is also observed in the Auger spectrum coincident with $Xe^{4+}$ ions (blue curve in Fig. 5), where the intensity of the peak structure is almost equal to that in the total Auger spectrum. This implies that the decay of these states mainly leads to the formation of $Xe^{4+}$ levels, while the $4d^{-2}$ satellite states lie above the $Xe^{5+}$ threshold. The energy correlations between the two Auger electrons emitted in the decay from the $4d^{-2}$ satellites (see Fig. 6(b)) show structures that are formed by the transitions of $4d^{-2}$ satellites $\rightarrow 4d^{-1}5l^{-2} \rightarrow 5l^{-4}$. These islands reflect the dense distribution of $4d^{-2}$ satellites and are observed less distinctly than those in Fig. 6(a). The first-step transitions of $4d^{-2}$ satellites $\rightarrow 4d^{-1}5l^{-2}$ emit Auger electrons in the kinetic energy range of 40–50 eV, and the associated structures lie below the $4d^{-2}$ satellite peak in the coincidence Auger spectrum (blue curve in Fig. 5). A reliable estimate of the net intensity of the CK transition to the $4d^{-2}$ satellites can be obtained from the total intensity of the island structures due to the stepwise decay of $4d^{-2}$ satellites. The total intensity of the island structures in Fig. 6(b) is about one-fifth of that shown in Fig. 6(a), and which implies for the 4s decay a branching ratio of $Xe^{4+}$ formation *via* $4d^{-2}$ satellites of about 6%. The processes that have been linked with $Xe^{4+}$ production account for only ~40% of the 4s decay, while the remaining ~15%, *i.e.*, the difference from the branching ratio of total $Xe^{4+}$ formation (55%), should presumably be attributed to processes that follow the $N_1N_{2,3}O_{1,2,3}$ CK transitions to the $4p^{-1}5l^{-1}$ states.

The Auger spectrum coincident with the $Xe^{5+}$ ion (green curve in Fig. 5) shows a gradual increase in intensity as the kinetic energy decreases, and weakly embeds shape peaks around a kinetic energy of 10 eV. The electron distribution extends up to a kinetic energy of 45 eV. Here, the energy level

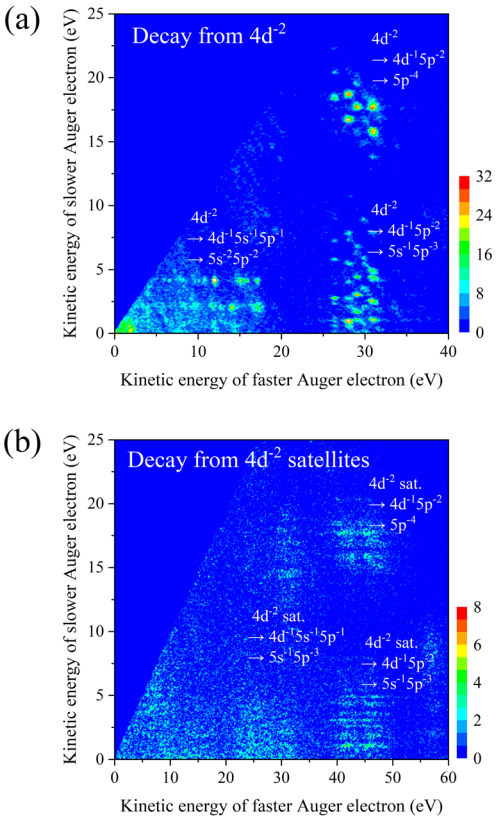


Fig. 6 Two-dimensional maps showing energy correlations between two Auger electrons emitted in the decay from (a) $4d^{-2}$ and (b) $4d^{-2}$ satellites, which are obtained from five-fold coincidences including the 4s photoelectron, CK electron and $Xe^{4+}$ ion.

diagram in Fig. 3 suggests that only the transition of $4s^{-1} \rightarrow 4d^{-2}$ satellites can emit such high-energy electrons along the path to the final formation of $Xe^{5+}$, implying that a small fraction of the $4d^{-2}$ satellites finally emits a total of three electrons. It is estimated from the coincidence counts in the kinetic energy range of 38–45 eV that the subsequent decay path of the $4d^{-2}$ satellites forms at most a 1% fraction of the 4s decay. It is very likely that the $N_1N_{2,3}O_{1,2,3}$ CK transitions to $4p^{-1}5l^{-1}$ and the subsequent decays with three electron emission are the main pathways to the Auger spectrum coincident with $Xe^{5+}$, though the overlap of structures associated with different decay steps prevents us from isolating the CK structures in this spectrum. A detailed inspection of the correlated energies of Auger electrons could yield information on quadruple Auger decay pathways but such an analysis is beyond the scope of this study.

## V. Conclusions

The Auger decay of the Xe 4s core-hole state was studied by multi-electron–ion coincidence spectroscopy using a magnetic bottle electron spectrometer. The first-step Auger decay included several CK transitions and an SCK transition, whose branching ratios were determined from the intensities of the

 

corresponding Auger structures. Information on the energy correlations between the emitted electrons enabled us to identify subsequent transitions that formed double, triple, and quadruple Auger pathways. A further coincidence with product ions helped to isolate the Auger structures relevant to the formation of individual charge states. The present work demonstrates that further coincidence with the product ion enhances the power of multi-electron coincidence measurements and helps to elucidate complicated Auger decay processes.

## Author contributions

Y. H. performed the measurements and data analysis; S. F. performed the calculation; Y. H. drafted the manuscript, which was completed in consultation with S. F.

## Conflicts of interest

There are no conflicts to declare.

## Acknowledgements

This work was performed at the UVSOR Synchrotron Facility with the approval of the Institute for Molecular Science (proposal numbers 20-752 and 21-654). The author is grateful to the UVSOR staff for the stable operation of the UVSOR-III storage ring. This work was supported in part by JSPS KAKENHI (Grant number 21K03430), Research Foundation for Opto-Science and Technology, and the Matsuo Foundation.

## References

1 K. Okuyama, J. H. D. Eland and K. Kimura, *Phys. Rev. A: At., Mol., Opt. Phys.*, 1990, **41**, 4930.
2 J. H. D. Eland, O. Vieuxmaire, T. Kinugawa, P. Lablanquie, R. I. Hall and F. Penent, *Phys. Rev. Lett.*, 2003, **90**, 053003.
3 F. Penent, J. Palaudoux, P. Lablanquie, L. Andric, R. Feifel and J. H. D. Eland, *Phys. Rev. Lett.*, 2005, **95**, 083002.
4 P. Lablanquie, L. Andric, J. Palaudoux, U. Becker, M. Braune, J. Viefhaus, J. H. D. Eland and F. Penent, *J. Electron Spectrosc. Relat. Phenom.*, 2007, **156–158**, 51.
5 Y. Hikosaka, P. Lablanquie, F. Penent, T. Kaneyasu, E. Shigemasa, J. H. D. Eland, T. Aoto and K. Ito, *Phys. Rev. A: At., Mol., Opt. Phys.*, 2007, **76**, 032708.
6 J. Palaudoux, P. Lablanquie, L. Andric, K. Ito, E. Shigemasa, J. H. D. Eland, V. Jonauskas, S. Kučas, R. Karazija and F. Penent, *Phys. Rev. A: At., Mol., Opt. Phys.*, 2010, **82**, 043419.
7 E. Andersson, S. Fritzsche, P. Linusson, L. Hedin, J. H. D. Eland, J.-E. Rubensson, L. Karlsson and R. Feifel, *Phys. Rev. A: At., Mol., Opt. Phys.*, 2010, **82**, 043418.
8 P. Lablanquie, S.-M. Huttula, M. Huttula, L. Andric, J. Palaudoux, J. H. D. Eland, Y. Hikosaka, E. Shigemasa, K. Ito and F. Penent, *Phys. Chem. Chem. Phys.*, 2011, **13**, 18355.
9 I. H. Suzuki, Y. Hikosaka, E. Shigemasa, P. Lablanquie, F. Penent, K. Soejima, M. Nakano, N. Kouchi and K. Ito, *J. Phys. B: At., Mol. Opt. Phys.*, 2011, **44**, 075003.
10 Y. Hikosaka, T. Kaneyasu, P. Lablanquie, F. Penent, E. Shigemasa and K. Ito, *Phys. Rev. A: At., Mol., Opt. Phys.*, 2015, **92**, 033413.
11 Y. Hikosaka, P. Lablanquie, F. Penent, T. Kaneyasu, E. Shigemasa, J. H. D. Eland, T. Aoto and K. Ito, *Phys. Rev. Lett.*, 2007, **98**, 183002.
12 G. Wendin and M. Ohno, *Phys. Scr.*, 1976, **14**, 148.
13 J. H. D. Eland, C. Slater, S. Zagorodskikh, R. Singh, J. Andersson, A. Hult-Roos, A. Lauer, R. J. Squibb and R. Feifel, *J. Phys. B: At., Mol. Opt. Phys.*, 2015, **48**, 205001.
14 Y. Hikosaka, *J. Electron Spectrosc. Relat. Phenom.*, 2022, **255**, 147158.
15 S. Svensson, N. Mårtensson, E. Basilier, P.-Å. Malmquist, U. Gelius and K. Siegbahn, *Phys. Scr.*, 1976, **14**, 141.
16 Y. Hikosaka, M. Sawa, K. Soejima and E. Shigemasa, *J. Electron Spectrosc. Relat. Phenom.*, 2014, **192**, 69.
17 Y. Hikosaka and E. Shigemasa, *Int. J. Mass Spectrom.*, 2019, **439**, 13.
18 S. Fritzsche, *Comput. Phys. Commun.*, 2019, **240**, 1.
19 I. P. Grant, Relativistic Quantum Theory of Atoms and Molecules, *Springer Series on Atomic, Optical, and Plasma Physics*, Springer, New York, 2007.
20 S. Schippers, M. Martins, R. Beerwerth, S. Bari, K. Holste, K. Schubert, J. Viefhaus, D. W. Savin, S. Fritzsche and A. Müller, *Astrophys. J.*, 2017, **849**, 5.
21 S. Fritzsche, G. Zschornack, G. Musiol and G. Soff, *Phys. Rev. A: At., Mol., Opt. Phys.*, 1991, **44**, 388.
22 S. Schippers, A. Borovik Jr., T. Buhr, J. Hellhund, K. Holste, A. L. D. Kilcoyne, S. Klumpp, M. Martins, A. Müller, S. Ricz and S. Fritzsche, *J. Phys. B: At., Mol. Opt. Phys.*, 2015, **48**, 144003.
23 M. H. Chen, B. Crasemann, N. Martensson and B. Johansson, *Phys. Rev. A: At., Mol., Opt. Phys.*, 1985, **31**, 556.
24 S. Fritzsche, P. Palmeri and S. Schippers, *Symmetry*, 2021, **13**, 520.
25 S. Fritzsche, B. Fricke and W.-D. Sepp, *Phys. Rev. A: At., Mol., Opt. Phys.*, 1992, **245**, 1465.
26 Z. Liu, Q. Liu, Y. Ma, F. Zhou and Y. Qu, *Chin. Phys. Lett.*, 2021, **38**, 023201.
27 A. G. Kochur, A. I. Dudenko, V. L. Sukhorukov and I. D. Petrov, *J. Phys. B: At., Mol. Opt. Phys.*, 1994, **27**, 1709.
28 A. Kramida, Yu Ralchenko and J. Reader, NIST ASD Team, 2020. NIST Atomic Spectra Database (ver. 5.8). Available: **https://physics.nist.gov/asd**.